Wall-modeled LES: Recent applications to complex flows

By G. I. Park AND P. Moin

1. Motivation and objectives

Wall modeling for large-eddy simulation (LES) of high-Reynolds-number wall-bounded turbulent flows has been receiving growing attention in the CFD community in recent years. The fundamental reason that LES requires wall models in high-Reynolds-number flows is the prohibitive cost of wall-resolved LES, and the inaccuracy of the currently available subgrid-scale (SGS) models on coarse grids. The state-of-the-art SGS models, including dynamic models, provide insufficient SGS stress in coarse grids (Jiménez & Moser 2000; Sayadi & Moin 2012), so that accurate LES often requires most scales of the stress-generating motions to be resolved directly. As scale separation between the energy-containing motions and the smallest dissipative eddies diminishes progressively toward the wall, wall-resolved LES at many times is as costly as direct numerical simulation, often going beyond the capacity of current supercomputers. Wall modeling reduces the cost of LES to affordable levels by bypassing the computationally demanding inner portion of the boundary layer. Wall models are designed to augment the total shear stress in the near-wall region, which otherwise would be underpredicted significantly with the current SGS models on coarse grids.

This report summarizes the progress made this year toward applying wall-modeled LES (WMLES) to high-Reynolds-number complex flows, and identifies an open question and related technical challenge to be addressed in the coming years. We first report recent applications of LES with RANS-based wall models to flows over a wall-mounted hump and a model aircraft. The former is in fact a continuation of the work reported last year (Park 2015), but here emphasis is placed more on comparing the performance of wall models and analyzing the source of underperformance of a simple wall model in a flow with strong non-equilibrium effects. Investigation of the latter case has just begun, but the preliminary results warrant an early report, as this is presumably the first application of the standard LES methodology deploying explicit SGS models and low-dissipation numerics to a truly complex, external-aerodynamics configuration at a moderately high Reynolds number. The second part of the report identifies an open question associated with the placement of the so-called matching location in WMLES, where LES information is extracted and prescribed on wall-stress models as boundary conditions.

2. Flow solver and wall models

The details regarding the flow solver and wall models used in the present study are documented in Park & Moin (2014, 2016*a*) and Bodart & Larsson (2011); hence, only a brief summary is given below. In the present study, we use the flow solver CharLES, developed at CTR and Cascade Technologies, Inc., which solves the filtered compressible Navier-Stokes equations on unstructured grids with a cell-centered finite volume discretization.

A third-order explicit Runge-Kutta scheme is used for the time advancement. The spatial scheme is formally second-order accurate. For the discretization (reconstruction) of the advection terms, the non-dissipative central flux is blended with the dissipative upwind flux, where the proportion of the upwind flux scales with local departure of the global advection operator from a skew symmetric matrix. This ensures that the code generally operates with very low numerical dissipation except in the regions of poor grid quality and shocks.

We consider two standard zonal wall-stress models in the present work: a non-equilibrium wall model (NEQWM) and an equilibrium stress wall model (EQWM). Details regarding the wall-model equations, implementation, and their validations are documented in Park & Moin (2014, 2016*a*,*b*), Bodart & Larsson (2011), and Bodart *et al.* (2013); hence, only a brief summary is given here. In both approaches, the LES equations are solved on coarse grids where use of the no-slip wall boundary condition is no longer adequate. The stress boundary conditions, obtained from the wall models, are applied at the wall instead. The wall models solve simplified or full Navier-Stokes equations on a separate near-wall domain. The wall-model domain is often taken to be a small fraction of the local boundary layer thickness (e.g., 0.1δ). The instantaneous LES data and the no-slip condition are enforced on the top and wall boundaries of the wall models, respectively. At each time step, the viscous stress and the heat flux required to update the wall-adjacent LES solution are obtained directly from the wall-model solution. The wall-model grid has fine resolution in the wall-normal direction to impose the no-slip wall condition, but it usually maintains the same wall-parallel mesh content as that of the primal LES grid.

The NEQWM solves the unsteady three-dimensional RANS equations on a separate near-wall grid. The wall-model equations therefore have the same form as that of the primal LES. RANS parameterization of the unresolved turbulence in the wall model is natural, because only the statistical ensemble of the unresolved eddies can be represented with very large lateral grid spacings and time steps (Piomelli & Balaras 2002). We deploy a mixing-length turbulence model with a dynamic correction, which excludes the proportion of the resolved fluctuations in the NEQWM from the modeled stress (Park & Moin 2014).

The EQWM assumes the presence of an equilibrium boundary layer in which the total shear stress is in equilibrium with the wall-shear stress (Degraaff & Eaton 2000). This assumption is equivalent to neglecting all the terms in the NEQWM except for the wall-normal diffusion. The EQWM then reduces to a simple system of two coupled ordinary differential equations (ODEs) for each wall face that is solved along the wall-normal direction (Wang & Moin 2002; Bodart & Larsson 2011; Kawai & Larsson 2012). These equations are solved on a one-dimensional grid defined implicitly along the local wall-normal direction. The solution procedure involves inversions of the tri-diagonal systems obtained from one-dimensional finite-volume discretization of the ODEs, and therefore the EQWM is computationally efficient.

3. Complex flow applications

3.1. *A flow over a wall-mounted hump*

This work complements the investigation reported in Park (2015), where a high Reynolds number separating and reattaching flow over the NASA wall-mounted hump was predicted with WMLES. The chord Reynolds number is only moderately high ($\mathrm{Re}_c =$

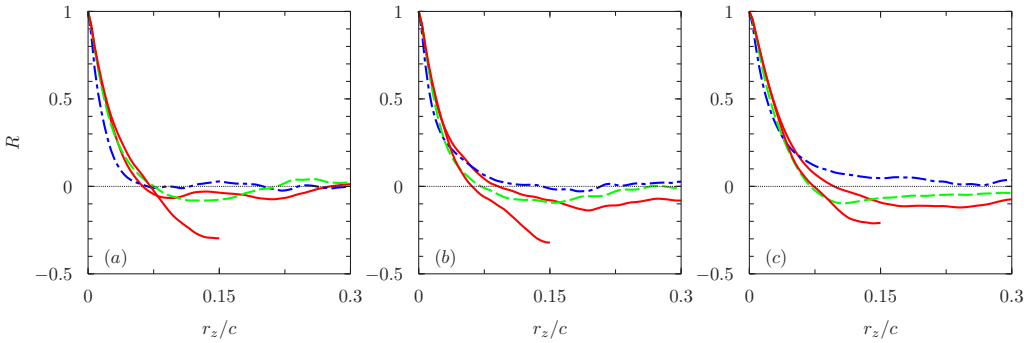

FIGURE 1. Spanwise autocorrelations of the streamwise (red solid lines), vertical (blue dash–dotted line), and spanwise (green dashed line) velocities from WMLES with the EQWM. The correlations are calculated near the center of the separation bubble at (*a*) $(x, y) = (0.915, 0.052)$, (*b*) $(x, y) = (0.915, 0.11)$, and (*c*) $(x, y) = (1.1, 0.052)$. For the simulation with a short spanwise domain ($L_z/c = 0.3$), only the streamwise velocity correlations (which extend up to $r_z/c = 0.15$) are shown.

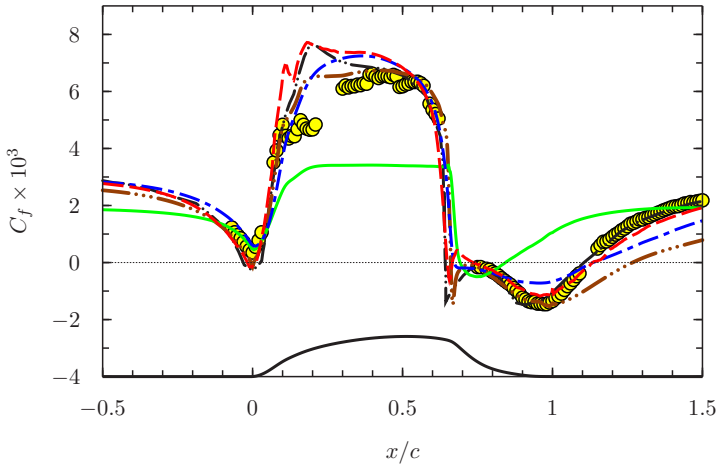

FIGURE 2. Skin friction coefficient along the bottom wall. Lines are from the simulations run with the baseline grid (G1). Red dashed line, LES with the NEQWM; blue dashed-dotted line, LES with the EQWM; green solid line, no-slip LES; black dash-double-dotted line, resolved LES (You *et al.* 2006); brown dash-triple-dotted line, 2-D RANS with Spalart-Allmaras one-equation model (Rumsey 2016); circles, experiment (Greenblatt *et al.* 2006).

0.93M), but the local friction Reynolds number in the attached-flow regions is sufficiently high to justify the use of wall models ($\mathrm{Re}_\tau = 2000 \sim 7000$). An important update from the last year's investigation is the increase of the spanwise computational domain size, L_z. Examination of the spanwise autocorrelations of the velocity components close to the separation bubble revealed that the spanwise domain size used in the previous report ($L_z/c = 0.3$) was too restrictive. As a result, all calculations reported in the previous report (Park 2015) were rerun with a larger spanwise domain ($L_z/c = 0.6$), where sufficient decays of the correlation coefficients are observed (Figure 1). The grid in the $x - y$ plane (z is the spanwise direction) is identical to the coarse grid G1 used in Park (2015). Two wall models described earlier (NEQWM and EQWM) are used.

Figure 2 compares the skin friction coefficients ($C_f = 2\tau_w/\rho U_\infty^2$) from the present cal-

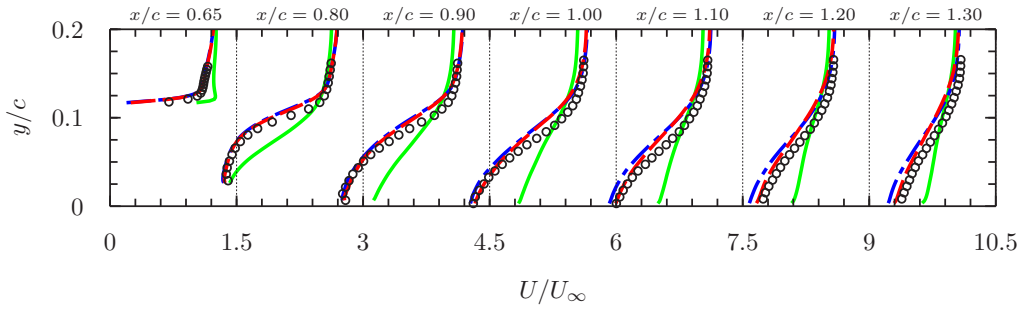

FIGURE 3. The mean velocity profiles from simulations run with the baseline grid (G1). Red dashed line, LES with the NEQWM; blue dashed-dotted line, LES with the EQWM; green solid line, no-slip LES; circles, experiment Greenblatt *et al.* (2006). Profiles are shifted along the abscissa by multiples of 1.5.

culations to the measurement (Greenblatt *et al.* 2006), a 2-D RANS calculation (Rumsey 2016), and a resolved LES result (You *et al.* 2006). Figure 3 compares the mean streamwise velocity profiles from the current study with the experiment. The no-slip LES (i.e., no wall model) results deviate significantly from the reference data, demonstrating that the LES grid G1 is too coarse for direct application of the no-slip wall boundary condition. The use of wall models greatly improves the skin friction and mean velocity predictions. The difference between the two wall models is most pronounced in the separated and recovery regions. In these regions ($x/c > 0.8$), agreement with the experiment is better in the NEQWM than in the EQWM. In the pre-separation region on the hump ($0 < x/c < 0.6$), C_f from the NEQWM deviates from the experimental data slightly more than the C_f from the EQWM does, but this minor difference has a negligible influence on the mean velocity development up to the separation point. Last, although not shown for brevity, little difference was found within the zero-pressure gradient flat-plate portion ($x/c < -0.7$), as expected.

The source of underperformance of the EQWM in the separated and recovery regions is further analyzed by quantifying the non-equilibrium contributions neglected in the EQWM, and by examining the validity of the constant-stress layer assumption. This would, in principle, require an *a-priori* analysis of flow fields obtained with fully resolved simulations as in the work of Hickel *et al.* (2012), but such analysis is infeasible in the present study due to the high Reynolds number. Instead, our analysis is based on the NEQWM solution from the present study. This *a posteriori* analysis still has a practical value by elucidating how certain simplifying assumptions can manifest into the skin friction error in actual WMLES computations.

For this analysis, we use the incompressible form of the NEQWM equation. This is legitimate, because the Mach number is less than 0.1 and the density variation is within 0.5% of the reference state in the domain of the NEQWM. The time and spanwise-averaged streamwise momentum equation in the NEQWM can be rearranged in the form of the EQWM as

$$\left\langle \frac{\partial}{\partial y}\left[(\nu + \nu_{t,wm})\frac{\partial u}{\partial y}\right]\right\rangle = S_1, \tag{3.1}$$

where the non-equilibrium source term S_1 at the right-hand side is defined as the sum

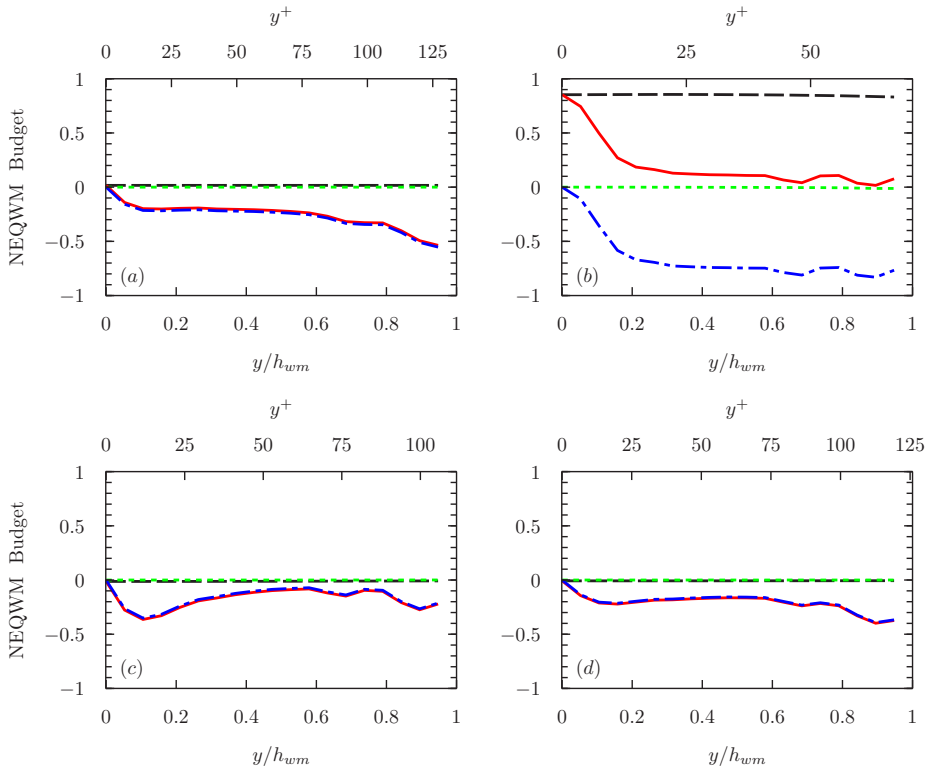

FIGURE 4. Budget of the mean streamwise momentum equation in the NEQWM as functions of the wall-normal distance normalized by the wall-model layer thickness (h_{wm}) and viscous wall unit (ν/u_τ). Blue dash-dotted line, advection (A_1); black long dashed line, pressure gradient (P_1); green short dashed line, lateral diffusion (V_1); red solid line, total non-equilibrium source ($S_1 = A_1 + P_1 - V_1$). (*a*) $x/c = -0.8$; (*b*) $x/c = 1$; (*c*) $x/c = 1.5$; (*d*) $x/c = 2$. The budget terms are normalized with the hump chord (c) and the free-stream velocity (U_∞).

of the following terms ($S_1 = A_1 + P_1 - V_1$)

$$\text{advection} \qquad A_1 = \frac{\partial \langle u \rangle^2}{\partial x} + \frac{\partial \langle u \rangle \langle v \rangle}{\partial y} + \frac{\partial \langle u' \rangle^2}{\partial x} + \frac{\partial \langle u' v' \rangle}{\partial y}, \tag{3.2}$$

$$\text{pressure gradient} \qquad P_1 = \frac{1}{\rho} \frac{\partial \langle P \rangle}{\partial x}, \tag{3.3}$$

$$\text{lateral diffusion} \qquad V_1 = \left\langle \frac{\partial}{\partial x} \left[(\nu + \nu_{t,wm}) \frac{\partial u}{\partial x} \right] \right\rangle. \tag{3.4}$$

Figure 4 shows the profiles of the above NEQWM budget terms at four streamwise stations: at an attached region upstream of the hump ($x/c = -0.8$), within the separation bubble ($x/c = 1$), and in the recovery region ($x/c = 1.5$ and 2). Note that the non-equilibrium contribution S_1 is non-zero everywhere. Streamwise diffusion is negligibly small in all regions, as expected. Pressure gradient is nearly constant along the wall-normal direction. In the attached regions, advection has the predominant contribution, and all other terms are negligible. At $x/c = 2$, the flow in the NEQWM has recovered from separation to exhibit a budget distribution similar to that in the upstream attached region. The characteristics in the separated region differ distinctly from those in the attached regions. Pressure gradient and advection have a significantly larger contribution

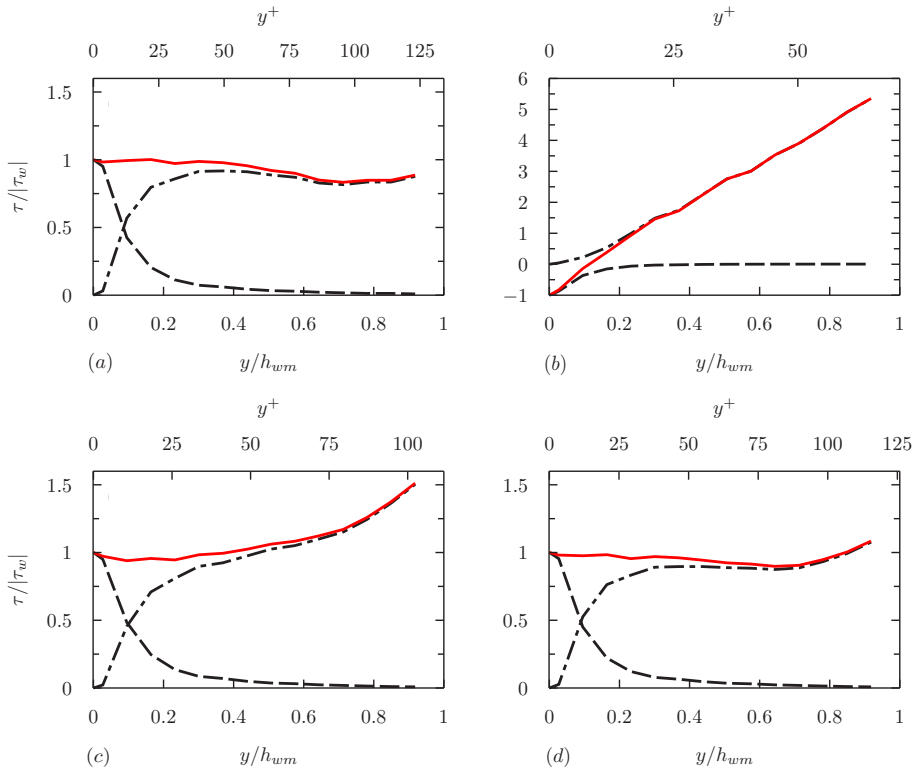

FIGURE 5. Profiles of the shear stresses in the NEQWM as functions of the wall-normal distance normalized by the wall-model thickness (h_{wm}) and viscous wall unit (ν/u_τ). Dashed line, viscous shear stress ($\langle\mu\partial u/\partial y\rangle$); dash dotted line, turbulent shear stress ($\langle\mu_{t,wm}\partial u/\partial y\rangle - \langle u'v'\rangle$); red solid line, total shear stress (viscous + turbulent). (*a*) $x/c = -0.8$; (*b*) $x/c = 1$; (*c*) $x/c = 1.5$; (*d*) $x/c = 2$.

throughout the inner portion of the separation bubble ($x/c = 1$). These terms largely balance each other, except in close vicinity to the wall where the advection vanishes due to the no-slip condition.

On the basis of the budget analysis, it can now be further deduced how the wall-shear stress in the NEQWM would change by omitting the non-equilibrium contribution S_1, as is done in the EQWM. Integrating Eq. (3.1) at a fixed streamwise location in the vertical direction (from the wall to the matching location $y = h_{wm}$), the following expression for the wall-shear stress in the NEQWM is

$$\tau_w = \left\langle (\mu + \mu_{t,wm})\frac{\partial u}{\partial y}\right\rangle_{y=h_{wm}} + \rho\int_0^{h_{wm}} -S_1(y)dy. \tag{3.5}$$

From Figure 4, the second term in Eq. (3.5) has positive and negative contributions to τ_w in the attached and separated regions, respectively. Therefore, neglecting S_1 (i.e., EQWM) would result in under- and overprediction of τ_w in the attached and separated regions, respectively. This result is consistent with the trend of the skin friction from the EQWM, compared to that from the NEQWM (for instance, see Figure 2 at $x/c = 1$ and 1.5).

The validity of the EQWM assumption can be also assessed through the profiles of the

total shear stress from the NEQWM. Recall that the EQWM by construction assumes that the sum of the viscous and turbulent shear stresses is constant along the wall-normal direction. Figure 5 shows the profiles of the shear stresses at the same streamwise stations as those considered in Figure 4. As expected, the equilibrium assumption seems reasonable in the upstream attached region ($x/c = -0.8$) and in the recovery region far downstream of the reattachment point ($x/c = 2$). However, the constant total stress assumption ceases to hold within the separation bubble and close to the reattachment, where considerable total stress gradients are found.

3.2. *NASA Common Research Model*

A validation study for assessing the predictive capability of the current WMLES techniques in a realistic external aerodynamics configuration was initiated during the 2016 CTR Summer Program, where preliminary WMLES calculations of a 3-D aircraft flow were carried out in collaboration with a participant with expertise in unstructured-grid LES and 3-D mesh generation (Lehmkuhl *et al.* 2016). The test case considered here is the NASA Common Research Model (CRM). It is a laboratory-scale aircraft model, but still possesses essential components in commercial airliners such as nacelle and pylon. The NASA CRM has served as a common test case for the state-of-the-art RANS codes in the recent AIAA CFD Drag Prediction Workshops (DPWs). The geometry we chose is the wing-body-nacelle-pylon (WBNP) configuration with a wind-tunnel-measured wing twist at a 4° angle of attack. The geometry accounting for the measured aeroelastic wing deformation was taken from the 6th DPW website (https://aiaa-dpw.larc.nasa.gov/) (Figure 6(a)). WMLES prediction of a flow at $\mathrm{Re} = 5 \cdot 10^6$ and $\mathrm{M} = 0.85$ is compared to the wind tunnel measurements from the Ames 11-ft wind tunnel and the Langley National Transonic Facility (NTF). Here Re denotes the Reynolds number based on the mean aerodynamic chord of the CRM wing and the free-stream velocity. M denotes the free-stream Mach number. The highest Re achieved in the experiments is about $30 \cdot 10^6$, but here we consider the lowest Re for initial assessment. The flow at $\mathrm{Re} = 5 \cdot 10^6$ still exhibits rich non-equilibrium aspects, including weak-shock on the suction surface interacting with wing boundary layer, mean spanwise flow motion due to the swept wing, juncture flows (wing-body and wing-nacelle-pylon), and separation.

A Voronoi mesh tool developed by Cascade Technologies, Inc., is used to automate the otherwise cumbersome grid-generating process. This tool generates a unique Voronoi tessellation of the computational domain out of a given point cloud. For the present investigation, we used the cell center coordinates from a full tetrahedra mesh (courtesy of Dr. Lehmkuhl, Lehmkuhl *et al.* (2016)) constructed with a commercial tool (ICEM CFD by Ansys, Inc.) as the point cloud input to the Voronoi mesh tool. A very coarse Voronoi grid with 12 million control volumes was constructed using 32 cores, taking less than an hour in wall-clock time. This mesh had approximately 5 cells across the wing boundary layer, and it is still too coarse to resolve the outer portion of the boundary layer. It is anticipated that a grid with $\mathrm{O}(10^9)$ cells will be required to comply with the standard resolution requirement for WMLES (Chapman 1979; Choi & Moin 2012). The two meshes (Voronoi and full tetrahedra) consequently had identical cell centroids, but the Voronoi mesh in general has superior mesh quality, as the cell face in most time perpendicularly crosses the line connecting the centroids of the neighboring cells at its midpoint. This property not only improves the accuracy of the central reconstruction scheme, but also enables stable calculations with a very low level of numerical dissipation. LES calculations with Voronoi meshes ran stably with a purely central scheme. On the

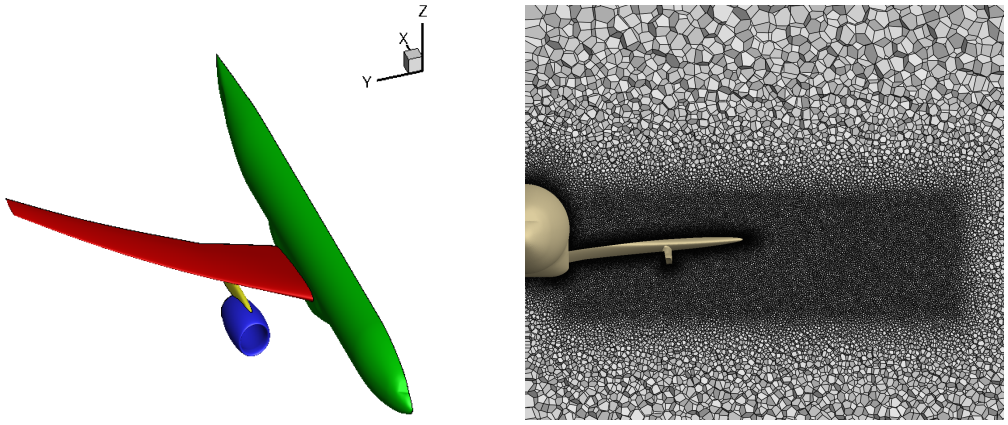

(*a*) (*b*)

FIGURE 6. (*a*) CRM geometry with wing, body, nacelle, and pylon. The computational domain includes a half aircraft attached to a symmetry plane. (*b*) Visualization of Voronoi mesh elements on a x-plane on the wing.

contrary, calculations with the full tetrahedra mesh blew up easily even with the full upwind treatment of the convective Euler flux.

A promising result was obtained from the preliminary calculation with a very coarse Voronoi mesh. Force prediction obtained with CharLES (equilibrium stress model, Voronoi mesh) is compared to the two wind tunnel measurements in Figure 7. Here, a prediction obtained with the code TermoFluids (Werner-Wengle wall model (Werner & Wengle 1993), tetrahedra mesh) (Lehmkuhl *et al.* 2016) is presented as well for a code-to-code comparison. The results from the two codes obtained with the coarse 12M-CV grids are comparable despite using different wall models, and their agreement with the experiments is excellent. Note that the no-slip LES (no wall model) calculation deviates clearly from the experiments. The fact that the refined calculation carried out with TermoFluids (103M CV) produces results quite close to the coarse calculation results is also promising, as WMLES predictions appear to be already largely converging at this grid resolution.

In the upcoming year, we plan to carry out additional calculations with increased grid resolutions and with different wall models. We envision having to use $O(10^9)$ cells to conform with the standard resolution requirement for WMLES in the literature (20∼30 cells in δ_{99} length in each direction). The idea is to compare the state-of-the-art wall models on the same configuration using a common code base. More detailed statistics such as local pressure distributions and velocity profiles on the wing and in the near wake will be collected and analyzed against the measurements.

4. Issue: accurate and robust local wall-modeling formulation

This section discusses a current standard in using RANS-based wall models, and issues arising when this rule is to be satisfied in complex flows.

A current standard in using the RANS-based or law-of-the-wall-based wall models is to use the LES data away from the wall as the wall-model input, rather than to conveniently use the first off-wall LES data. This practice, first advocated by Kawai & Larsson (2012), is based on the simple argument that the LES solution in the first few grid points near

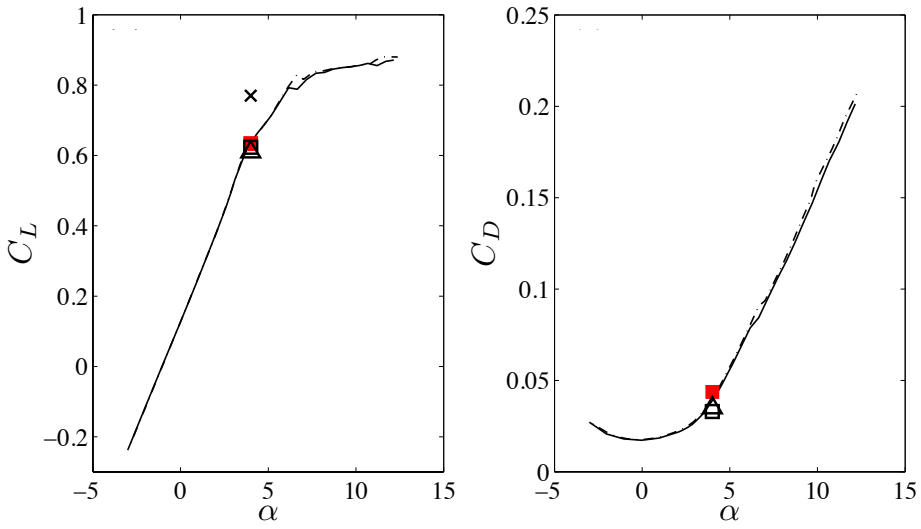

(*a*) (*b*)

FIGURE 7. Force prediction from (WM)LES obtained with different codes. (*a*) Lift. (*b*) Drag. Symbols indicate the following: cross, TermoFluids (12M tetrahedra, no-slip LES); empty square, TermoFluids (12M tetrahedra, Werner-Wengle wall model); filled square (red), CharLES (12M Voronoi, EQWM); triangle, TermoFluids (103M tetrahedra, Werner-Wengle wall model); solid lines, Ames 11-ft wind tunnel measurement (run t216R109); dashed lines, Langely NTF measurement (run t194R74).

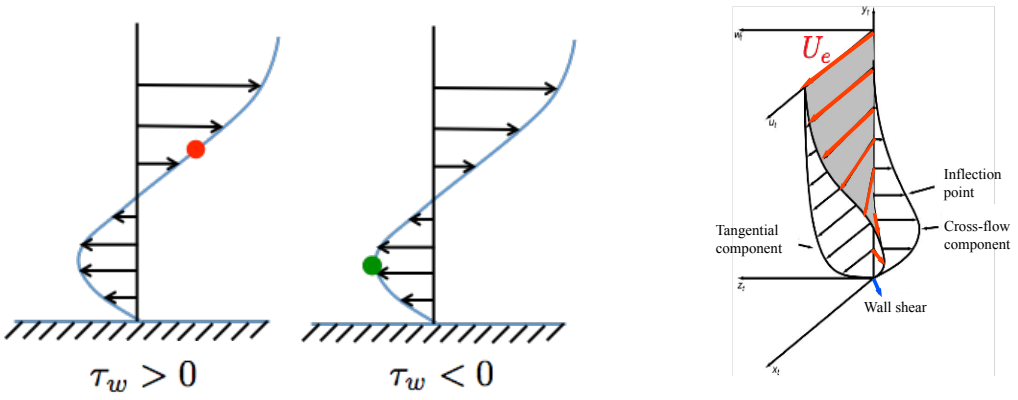

(*a*) (*b*)

FIGURE 8. Potential failure of non-local wall-modeling procedures using the LES input away from the wall. Some wall models can produce solutions with erroneous flow directions. (*a*) Separated flows. (*b*) Three-dimensional boundary layer with a skewed mean velocity profile.

the wall must be inherently contaminated by numerical and SGS modeling errors. They showed from their numerical experiments in high-Reynolds-number flat-plate boundary layers that the wall-shear stress and mean velocity were predicted accurately without the logarithmic-layer mismatch problem, when 1) the matching location was placed well within the log layer, and 2) at least three cells are placed within the LES grid below the matching location. A number of successful WMLES predictions of high-Reynolds-

number wall turbulence have in fact followed this guideline (Bodart & Larsson 2011; Kawai & Larsson 2012, 2013; Bodart *et al.* 2013; Park & Moin 2014; Park 2015; Park & Moin 2016*b*). While this third-point rule is now deemed an established practice in the literature, there is still a clear need to enable local wall-modeling procedure operating with the LES data at the first off-wall grid point (or cell). The matching location in principle is an implicit modeling parameter for many wall models, and one should expect some sensitivities of WMLES prediction to this parameter. This is especially true when simple wall models (e.g., log-law model, equilibrium stress model, and integral wall model) are used to treat the near-wall region exhibiting complex non-equilibrium effects. It can be trivially shown that these wall models can represent only monotonically varying velocity profiles within the wall-model domain, and that the LES flow direction at the matching location solely determines the direction of the wall-shear force. In separated flows or flows with mean three dimensionality, these wall models can easily produce the wall-shear stress with erroneous direction when operated with the third LES grid point data, as depicted in Figure 8. For these flows, it is therefore highly desirable to use the first off-wall grid point information for wall modeling, so that wall models always produce solutions with the correct flow direction in the near-wall region. It is emphasized that the situations depicted in Figure 8 are not pathological cases, as separated flows and the three-dimensional boundary layer are commonly found in a number of real-world applications such as the swept-wing boundary layer, juncture flow (e.g., wing-body junction), and atmospheric boundary layer.

In addition to potential inaccuracy in flows with complex velocity profiles, the third-grid-point matching approach when deployed in parallel, unstructured-grid LES solvers can incur non-trivial user overhead in model implementation and LES mesh preparation. First, communications between wall faces and their proper matching locations away from the wall requires a non-local search algorithm in the pre-processing stage, and potentially inter-processor data communications at each time step, which degrade parallel performance of the WMLES solver. More importantly, ensuring the existence of a proper matching location at the meshing stage is often impossible when complex geometries are meshed with unstructured elements. We encountered this issue in the CRM calculation presented earlier. Matching locations with a prescribed distance from the wall sometimes could not be located within the fluid domain near the wing-body and wing-pylon-nacelle junctions. Prevention of this problem at the meshing stage seems impractical, as it is very cumbersome to visually locate problematic mesh regions in complex geometries filled with unstructured elements. We simply reverted to the local wall-modeling approach using LES data in the wall control volumes.

Resolution of the log-layer mismatching problem in the local wall-modeling procedure requires first isolating its precise reason of failure beyond the loose numerical-error arguments made in Kawai & Larsson (2012). Unfortunately, this aspect is not well understood, partly due to the fact the log-layer mismatch with the first grid point wall modeling is not observed consistently in different codes. Kawai & Larsson (2012) reported overprediction of u^+ (underprediction of τ_w) in high-Reynolds-number boundary layers with their code using a sixth-order compact scheme with the equilibrium stress wall model. Lee *et al.* (2013) on the contrary reported underprediction of u^+ in their channel flow calculation at $\mathrm{Re}_\tau = 2000$ using a second-order staggered code with a log-law wall model.

One conjecture we have now is that the non-linear input-output relation in wall models, combined with the unsteadiness of the LES solution at the first off-wall grid point, works in a complicated manner to develop the log-layer mismatch problem. This view is first

supported by a numerically found, near-quadratic relation between the wall-model input (u_{LES}) and output (τ_w^{wm}). For instance, it was found from an *a-priori* analysis using the mean velocity profile from $\mathrm{Re}_\tau = 2000$ and 4000 channel DNS that $\tau_w^{wm} \sim u_{LES}^{1.8}$ in the log-law wall model and EQWM, as long as the matching location is placed in the logarithmic layer. Note that the equilibrium relation between the wall-model input/output after long-time integrations of fully coupled LES/wall-model equations is not known yet. This, however, still implies that not only the mean level of the LES velocity at the matching location but also the level of fluctuations therein may affect the wall-shear stress from the wall model. We currently envision exploring approaches to control the unsteadiness of the wall-model input (not manipulating the LES solution itself) and their effect on the wall-shear stress. These include, for example, filtering the wall-model input in space or time and introducing unsteady correction in simple types of wall models.

5. Conclusions

In the present study, complex flow applications of the WMLES techniques are presented. A high Reynolds number separating and reattaching flow over the NASA wall-mounted hump was revisited with a larger spanwise domain size. It was demonstrated that the comprehensive NEQWM consistently outperforms a simpler EQWM in the separated and recovery regions. A budget analysis of the NEQWM equations and examination of the stress equilibrium assumption revealed that key assumptions in the EQWM (i.e., negligible contribution of pressure gradient and unsteady advection, constancy of the total stress) are largely invalid in the separated and recovery regions. We also initiated an application of WMLES to a truly complex three-dimensional external aerodynamics configuration. Preliminary calculation with the EQWM yielded promising force prediction on a very coarse grid.

We have also identified a need for enabling local wall-modeling procedures. The current standard in WMLES of using the third point away from the wall as the wall-model input is potentially inaccurate in flows with separation and/or skewed mean velocity profiles. Additionally, ensuring the existence of a non-local matching point at a specified wall distance is often impossible in complex geometry meshed with unstructured elements. For this reason, it is important to develop a robust and accurate wall-modeling procedure using only the LES information in the wall-adjacent cells.

Acknowledgments

This work was supported by NASA under the Transformative Aeronautics Concepts Program, Grant #NNX15AU93A.

REFERENCES

Bodart, J. & Larsson, J. 2011 Wall-modeled large eddy simulation in complex geometries with application to high-lift devices. *Annual Research Briefs,* Center for Turbulence Research, Stanford University, pp. 37–48.

Bodart, J., Larsson, J. & Moin, P. 2013 Large eddy simulation of high-lift devices. *AIAA Paper* 2013–2724.

Chapman, D. R. 1979 Computational aerodynamics development and outlook. *AIAA J.* **17**, 1293.

Choi, H. & Moin, P. 2012 Grid-point requirements for large eddy simulation: Chapman's estimates revisited. *Phys. Fluids* **24**, 011702.

Degraaff, D. B. & Eaton, J. K. 2000 Reynolds-number scaling of the flat-plate turbulent boundary layer. *J. Fluid Mech.* **422**, 319–346.

Greenblatt, D., Paschal, K. B., Yao, C. S., Harris, J., Schaeffler, N. W. & Washburn, A. E. 2006 A separation control CFD validation test case, part 1: baseline and steady suction *AIAA Paper* 2004-2220.

Hickel, S., Touber, E., Bodart, J. & Larsson, J. 2012 A parametrized non-equilibrium wall-model for large-eddy simulations. *Annual Research Briefs,* Center for Turbulence Research, Stanford University, pp. 127–136.

Jiménez, J. & Moser, R. D. 2000 Large-eddy simulations: where are we and what can we expect? *AIAA J.* **38**, 605–612.

Kawai, S. & Larsson, J. 2012 Wall-modeling in large eddy simulation: length scales, grid resolution, and accuracy. *Phys. Fluids* **24**, 015015.

Kawai, S. & Larsson, J. 2013 Dynamic non-equilibrium wall-modeling for large eddy simulation at high Reynolds numbers. *Phys. Fluids* **25**, 015105.

Lee, J., Cho, M. & Choi, H. 2013 Large eddy simulations of turbulent channel and boundary layer flows at high Reynolds number with mean wall shear stress boundary condition. *Phys. Fluids* **25**, 110808.

Lehmkuhl, O., Park, G. I. & Moin, P. 2016 LES of flow over the NASA common research model with near-wall modeling. *Proceedings of the Summer Program,* Center for Turbulence Research, Stanford University, pp. 335–341.

Park, G. I. 2015 Wall-modeled large-eddy simulation of a separated flow over the NASA wall-mounted hump. *Annual Research Briefs,* Center for Turbulence Research, Stanford University, pp. 145–156.

Park, G. I. & Moin, P. 2014 An improved dynamic non-equilibrium wall-model for large eddy simulation. *Phys. Fluids* **26**, 015108.

Park, G. I. & Moin, P. 2016*a* Numerical aspects and implementation of a two-layer zonal wall model for LES of compressible turbulent flows on unstructured meshes. *J. Comput. Phys.* **305**, 589–603.

Park, G. I. & Moin, P. 2016*b* Space-time characteristics of wall-pressure and wall shear-stress fluctuations in wall-modeled large eddy simulation. *Phys. Rev. Fluids* **1**, 024404.

Piomelli, U. & Balaras, E. 2002 Wall-layer models for large-eddy simulations. *Annu. Rev. Fluid Mech.* **34**, 349–374.

Rumsey, C. L. 2016 *NASA Langley Research Center Turbulence Modeling Resource* https://turbmodels.larc.nasa.gov/nasahump_val_sa.html.

Sayadi, T. & Moin, P. 2012 Large eddy simulation of controlled transition to turbulence. *Phys. Fluids* **24**, 114103.

Wang, M. & Moin, P. 2002 Dynamic wall modeling for large-eddy simulation of complex turbulent flows. *Phys. Fluids* **14**, 2043–2051.

Werner, H. & Wengle, H. 1993 Large-eddy simulation of turbulent flow over and around a cube in a plate channel. *Turbulent Shear Flows* **8**, 155–168.

You, D., Wang, M. & Moin, P. 2006 Large-eddy simulation of flow over a wall-mounted hump with separation control. *AIAA J.* **44**, 2571–2577.